Available online at www.sciencedirect.com

SciVerse ScienceDirect

Ceramics International 38 (2012) 5585–5596

CERAMICS INTERNATIONAL

www.elsevier.com/locate/ceramint

Material characterization and bioactivity evaluation of dental porcelain modified by bioactive glass

Marianthi Manda [a], Ourania-Menti Goudouri [b], Lambrini Papadopoulou [c], Nikolaos Kantiranis [c], Dimitris Christofilos [d], Konstantinos Triantafyllidis [e], Konstantinos M. Paraskevopoulos [b], Petros Koidis [a,*]

[a] *Department of Fixed Prosthesis and Implant Prosthodontics, Dentistry School, Aristotle University of Thessaloniki, University Campus, Dentistry Building, GR 54124 Thessaloniki, Greece*
[b] *Physics Department, Aristotle University of Thessaloniki, University Campus, GR 54124 Thessaloniki, Greece*
[c] *School of Geology, Aristotle University of Thessaloniki, University Campus, GR 54124 Thessaloniki, Greece*
[d] *Physics Division, School of Technology, Aristotle University of Thessaloniki, University Campus, GR 54124 Thessaloniki, Greece*
[e] *Department of Chemistry, Aristotle University of Thessaloniki, University Campus, GR 54124 Thessaloniki, Greece*

Received 14 February 2012; received in revised form 31 March 2012; accepted 31 March 2012
Available online 7 April 2012

Abstract

This study aimed at the chemical, microstructural and textural characterization of the sol–gel derived dental porcelain modified by bioactive glass and the evaluation of its bioactivity. Sol–gel derived specimens of the composite material were constructed and subjected to firing cycle. Specimens of bioactive glass and dental porcelain served as control. All the specimens were characterized using X-ray diffraction (XRD), Raman spectroscopy, Fourier transform infrared spectroscopy (FTIR), scanning electron microscopy (SEM) coupled with energy dispersive spectroscopy (EDS) and N_2 porosimetry. The assessment of *in vitro* bioactivity was carried out by incubating the composite specimens in DMEM solution. Apatite formation was evaluated by SEM/EDS, FTIR and XRD analysis. Microstructural analysis by SEM revealed irregularly shaped particles with broad size distribution, while complex porei network with large pore volume and non-uniform pore size distribution was evident. N_2-adsorption isotherms were representative of non-nano-/meso-porous materials. A mixture of a- and b-wollastonite, apatite and leucite phases were detected by FTIR and Raman spectroscopy. The XRD analysis confirmed the previous results, though traces of cristobalite were identified too. The *in vitro* tests evidenced the bioactivity of the specimens in a 3-day-period. In conclusion, the physicochemical properties of the sol–gel derived composite result in a bioactive material, though further modifications need to be considered in order to fulfill the requirements of application in the clinical reality.

Keywords: A. Sol–gel process; D. Porcelain; D. Apatite; E. Biomedical applications

1. Introduction

The induction of bioactivity in dental porcelain material has been based on the preparation of bioactive glass-dental porcelain (BP) composite systems, aiming at the material's surface modification into a highly dissolved silicate network, able to induce a silica-rich gel layer [1]. This layer has been reported to promote the *in vitro* precipitation of apatite nano-film, which might *in vivo* be reformulated into a cementum-like interface, able to attach the periodontium [2]. Nevertheless, the surface reactivity of the aforementioned composites has been compromised by the high reaction temperature of the melting powder preparation technique, resulting in materials with high heterogeneity of the chemical structure and absence of porosity, whereas their surface area depended only on the particle size, obtained by grinding up the powders [3,4]. On the other hand, the application of low-temperature sol–gel process in the fabrication of bioactive ceramics allowed the control over the textural properties (specific surface area and porosity) and

---

* Corresponding author. Tel.: +30 2310 999659; fax: +30 2310 999676.
E-mail addresses: mgmanta21@yahoo.com (M. Manda), ogoud@physics.auth.gr (O.-M. Goudouri), lambrini@geo.auth.gr (L. Papadopoulou), kantira@geo.auth.gr (N. Kantiranis), christof@eng.auth.gr (D. Christofilos), ktrianta@chem.auth.gr (K. Triantafyllidis), kpar@auth.gr (K.M. Paraskevopoulos), pkoidis@dent.auth.gr (P. Koidis).

0272-8842/$36.00 © 2012 Elsevier Ltd and Techna Group S.r.l. All rights reserved.
http://dx.doi.org/10.1016/j.ceramint.2012.03.078

crystal structure, in order, not only to achieve an optimized bioactive surface [5], but to maintain surface bioactivity over a wider composition range of silica content [6–9]. Although the favorable processing parameters of the sol–gel method have been already applied on the preparation of BP composite systems [10], certain compositional limits and specific ratios of oxides in the BP systems, which may tailor the bioactivity of material, are still under investigation. Thus, the purpose of the present study was to study the chemical composition and the textural properties, along with the bioactivity, derived from the sol–gel preparation of a BP composite system, in a 50 wt% of oxides.

2. Materials and methods

The BP composite system was prepared by the sol–gel process [11]. In brief, the initial solution formation included the hydrolysis and polycondensation of tetra-ethoxy-silane (TEOS), tri-ethyl-phosphate (TEP) and calcium nitrate tetrahydrate ($Ca(NO_3)_2{\cdot}4H_2O$), which are the precursors of bioactive glass (B) 58S (SiO_2 60 wt%, CaO 36 wt% and P_2O_5 4 wt%). Dental porcelain (P) powder in the SiO_2–Al_2O_3–K_2O–Na_2O system, used for margin restoration of fixed partial dentures (IPS Inline-Margin Ceramic System, Ivoclar, Schaan, Liechtenstein), was added in the ratio of 50 wt%. Nitric acid was used to catalyze the TEOS and TEP hydrolysis. Each reactant was consequently added under continuous stirring. The sol–gel process was accomplished by the drying and firing cycles in a programmable furnace (Nabertherm, Germany), while the mixture remained at the stabilization temperature (700 °C) for 18 h. Pulverization by ball milling process and sieving of the mixture to a <40 μm-grained powder followed. Pure B 58S powder, which was also synthesized under the same sol–gel process parameters, along with the pure P powder, as it was received by the manufacturer, served as controls. All the powders were mixed with the modeling liquid of P (IPS Inline Margin, Build-Up Liquid, Ivoclar, Schaan, Liechtenstein) into a water-based thick slurry of the same viscosity. The resulting mixtures were molded, in polyvinyl-siloxane dies, into cylindrical disk specimens of 6 mm diameter and 1.5 mm height. During molding, the specimens were condensed, using vibration and drying technique, and they were removed from the moulds by gentle hand pressure. Disk specimens of B, P and BP material underwent firing cycle in the recommended furnace (Progamat P700, IVOCLAR Vivadent AG, Schaan, Liechtenstein) with a rate of 60 °C/min in vacuum and, finally, sintered at 930 °C for 1 min, according to manufacturer's recommendations for the firing cycle of P. All the specimens obtained were characterized for their (a) chemical composition and (b) textural properties. Disk specimens of BP material were further evaluated for their bioactive behavior.

Chemical composition evaluation was performed by: (a) scanning electron microscopy (SEM) and energy dispersive spectroscopy (EDS) (JEOL J.S.M. 840A, Tokyo, Japan) for microstructure and stoichiometric analysis, respectively, on the surface and cross-section of the disk specimens. The cross-sections were prepared by embedding the specimens in epoxy resin (Epofix resin, Struers), placing them in a vacuum chamber for 5 min, leaving to cure in room temperature for 24 h, cutting along the sagittal plane using a high speed microtome (Accutom II®, Struers), grinding, using 1200–4000 grit SiC disks in a grinding-polishing device (DAP-V®, Struers) and polishing them with diamond paste, (b) Fourier transformed infrared (FTIR) analysis, using a spectrometer (PerkinElmer Spectrometer Spectrum 1000) in transmittance mode and in the region of 400–2000 cm^{-1} for surface spectroscopic study after appropriate preparing the specimens using the KBr pellet technique, (c) micro-Raman spectroscopy, using a triple grating spectrometer system ("XY", Dilor, Lille, France) with an incorporated Olympus microscope and a liquid nitrogen-cooled CCD detector to record Raman spectra in a backscattering geometry. The 514.5 nm line of an Ar^+ laser was used for excitation at a power of $\sim$20 mW measured just before the microscope objective, and (d) X-ray diffraction (XRD) analysis using diffractometer (Philips_PW1710) with Ni-filtered Cu Kα radiation, at the scanning rate of $0.01^\circ\ 2\theta\ s^{-1}$ in the 2θ range of 5–75°, while the step size was 0.05° (2θ). Textural characterization was performed by nitrogen (N_2) adsorption–desorption experiments, after degassing the samples at 320 °C for 16 h under 5×10^{-9} Torr vacuum, using an Automatic Volumetric Sorption Analyzer at -196 °C (Autosorb-1MP, Quantachrome). The surface areas were calculated by the multi-point Brunauer–Emmett–Teller (BET) method and the total pore size distribution and volume (at $P/P_o = 0.99$) were calculated by the Barrett–Joyner–Halenda (BJH) method. The assessment of *in vitro* acellular bioactivity was carried out by immersing the disk BP specimens in serum-free Dulbecco's Modified Eagle's Medium (DMEM), containing penicillin (100 U/ml) and amphotericin (1.5 mg/ml), while the medium volume (ml)-to-specimen weight (mg) ratio was 2:3. Incubation at 37 ± 1 °C for 6 days followed. DMEM was renewed on the 6th hour, 1st, 3rd and 5th day after incubation and the specimens were removed the 6th hour, 1st, 3rd and 6th day. After the removal, the specimens were rinsed with ethanol and distilled water, dried and stored in airtight container. Bioactivity control was performed by evaluating the apatite layer formation on the specimens' surface, detected by: (a) FTIR in transmittance mode, (b) XRD, and (c) SEM/EDS analysis under the same parameters, previously described.

3. Results

3.1. Structural and chemical analysis

3.1.1. SEM/EDS analysis

Surface and cross-section SEM images of the B, P and BP control specimens' microstructure are presented in Figs. 1 and 2, respectively. SEM surface images of BP specimens (Fig. 1a and b) were characterized by a homogeneous surface, with coarse, flattened and rounded particles, while the cross-section SEM images (Fig. 2a and b) revealed irregularly shaped particles with broad size distribution. The internal pore architecture seemed to be quite complex with large pore volume and non-uniform pore size distribution. The SEM surface image of B specimens (Fig. 1c and d) was characterized

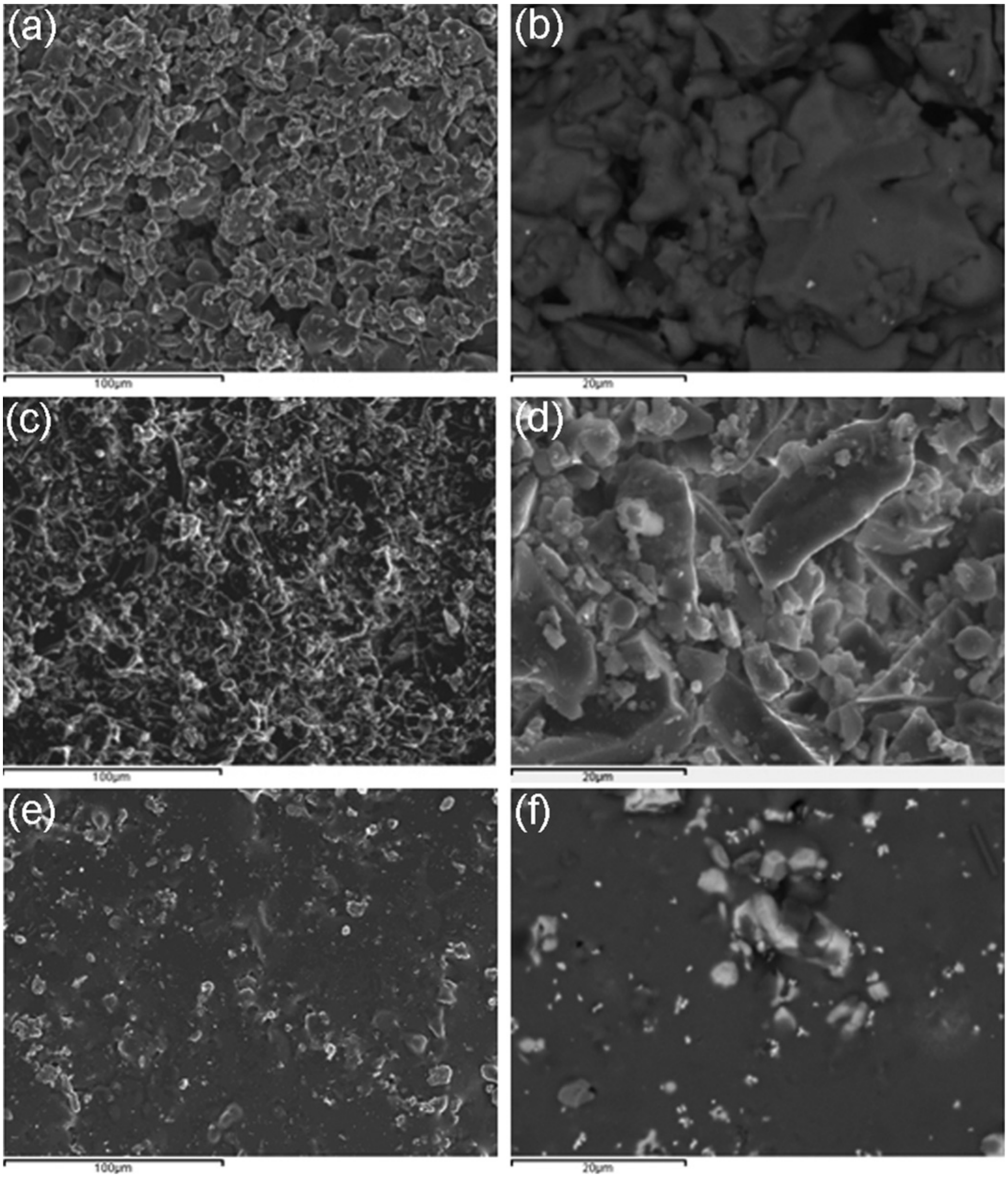

Fig. 1. Secondary (500×) (a, c, and e) and backscatter (1500×) (b, d, and f) electron surface analysis of the BP (a and b), B (c and d) and P (e and f) control specimens.

by well-defined, angular-shaped particles with platelet configuration. The microstructure appearing in the cross-section SEM images of B specimens (Fig. 2c and d) was similar to that of BP specimens, though the pore boundaries were quite undefined. On the contrary, P specimens presented considerably different SEM surface (Fig. 1e and f) and cross-section (Fig. 2e and f) images compared to the B and BP specimens, exhibiting an irregular, though, dense structure with low porosity. The EDS surface and cross-section stoichiometric analysis of BP specimens showed that the predominant elements were Si, followed by: (a) Ca and P and (b) K, Al and Na. Si, Ca and P were also detected in the B specimens, since they were included in the precursors of bioactive glass preparation, suggesting the presence of calcium–phosphate or calcium–silicate phases in the silicate substrate. Si, Al and K elements were also detected on the large grains of P specimens, suggesting the presence of silicate minerals. The trace bright grey areas in the backscattered image, on the surface of P specimens, contained Zr, Zn, Ti, Sn and Y, while small quantities of Ba, Ca and P were also detected.

3.1.2. FTIR and Raman analysis

FTIR spectra of all the control specimens are displayed in Fig. 3, while the relevant Raman spectra appear in Figs. 4 and 5. In particular, the calcium–phosphate phases were distinguished by the FTIR frequencies of the observed peaks, associated with the PO_4^{3-} internal modes, appearing in the region of the ν_4 bending mode of PO_4^{3}, exhibiting a double peak at 564 and 604 cm^{-1} (Fig. 3a and b) [11], which are typical for crystalline apatite-like phases. Furthermore, in the FTIR spectrum of BP and B specimens, the broad bands of the amorphous silicate matrix were clearly observed at: a. 400–550 cm^{-1}, assigned to

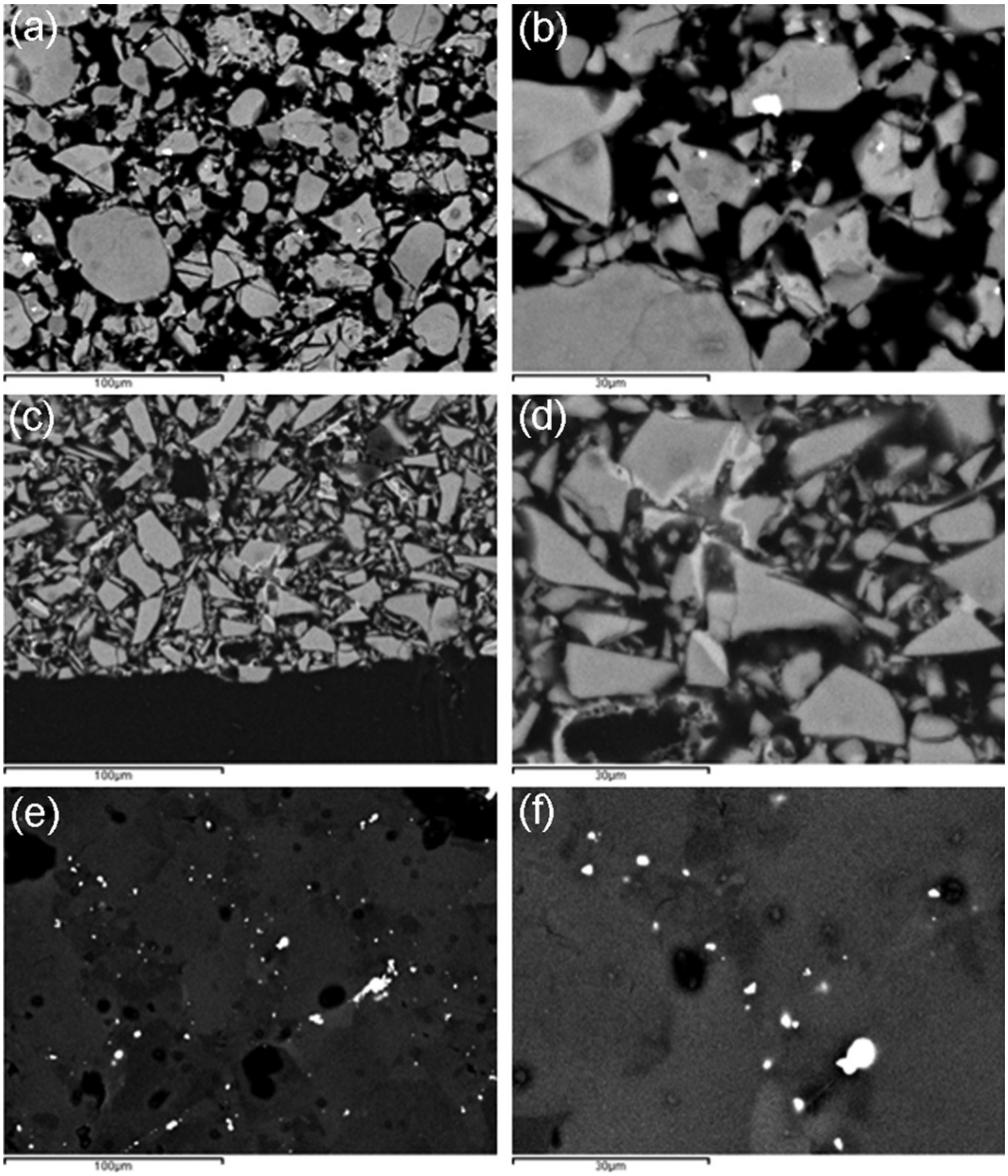

Fig. 2. Backscatter electron cross-section analysis 500× (a, c and e) and 1500× (b, d, and f) of the BP (a and b), B (c and d) and P (e and f) control specimens.

the Si–O–Si bending, (b) 850–1250 cm^{-1}, assigned to the Si–O stretching vibrations and (c) 800 cm^{-1}, related to the vibration motion of the bridging oxygens in a direction perpendicular to the Si–Si axis (Fig. 3a and b) [12]. Raman spectroscopy further confirmed the presence of the Ca–P phases on the surface of the BP control specimens, through the peak arising from the broad band in the region of the phosphate ν_4 bending mode, at 578 cm^{-1} (Fig. 4a and b) and the observed strong peak, appearing in the region of the phosphate ν_1 stretching mode, at 960 cm^{-1} (Fig. 4c) [13,14]. B control specimens (Fig. 5d and e) further exhibited the peak appearing in the region of phosphate ν_2 bending mode at 432–442 cm^{-1} (Fig. 4d) [13,14]. Indications of the Ca–P phases were also suggested by the peaks at 1041, 1071 and 1123 cm^{-1}, forming the broad band at the region of the ν_3 stretching mode (Fig. 4c and e) [13,14]. The Ca–Si phases crystallized on the BP and B surface, identified by FTIR, were the b-wollastonite and a- or pseudo-wollastonite. The appearance of 2 weak peaks at the 938 and 988 cm^{-1} in the B and BP FTIR spectra was assigned to the b-wollastonite, while the intense peak, at 716 cm^{-1}, was attributed to a-wollastonite (Fig. 3a and b) [15]. Raman spectroscopy also indicated the presence of wollastonite and a-wollastonite on the B specimens. b-Wollastonite was identified in the spectrum of the B specimens, by the shoulder at 970 cm^{-1} (Fig. 4f), attributed to the Si–O_{nbr} stretching mode, and the peak at 636 cm^{-1} (Fig. 4e), assigned to the Si–O_{br} [16]. However, in the spectrum of the BP specimens, the peak of b-wollastonite is not clearly distinguishable, due to its overlapping with the strong peak of apatite at 960 cm^{-1}. Pseudowollastonite was identified on the surface of the B specimen, by the shoulder at the 984 cm^{-1} (Fig. 4f) and the peak 575 cm^{-1} (Fig. 4e), in the relevant Raman spectrum [17]. The latter overlapped with the peak of apatite.

The contribution of dental porcelain on the phase crystallization of BP composite material was observed through the

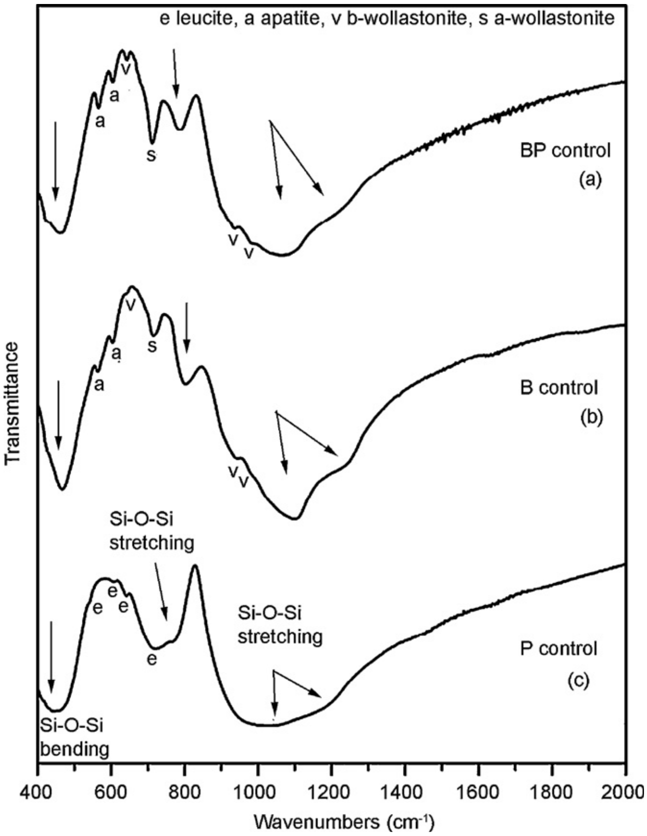

Fig. 3. FTIR analysis of the BP (a), B (b) and P (c) control specimens.

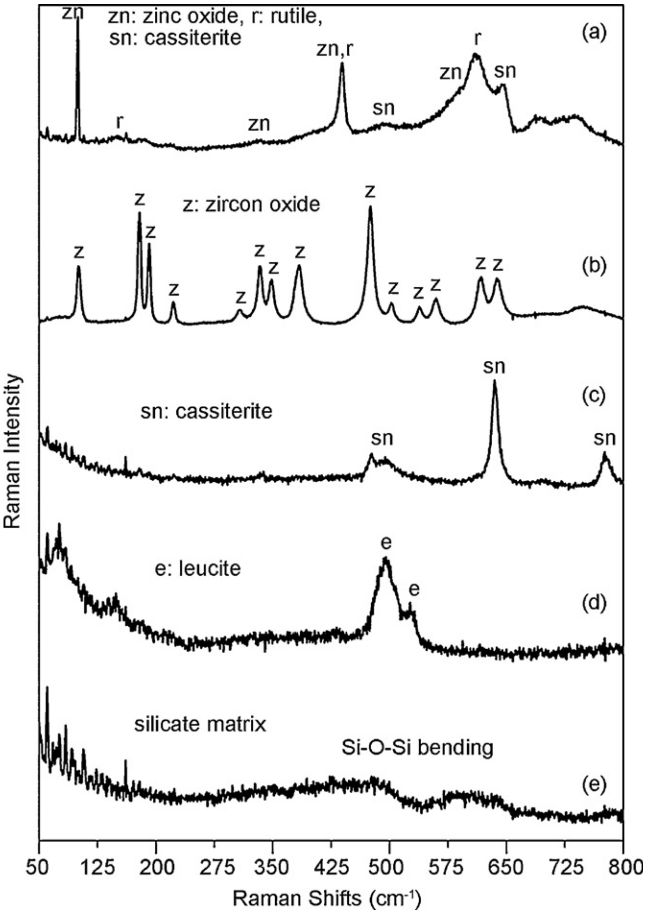

Fig. 5. Raman spectra of P (a–e) control specimen.

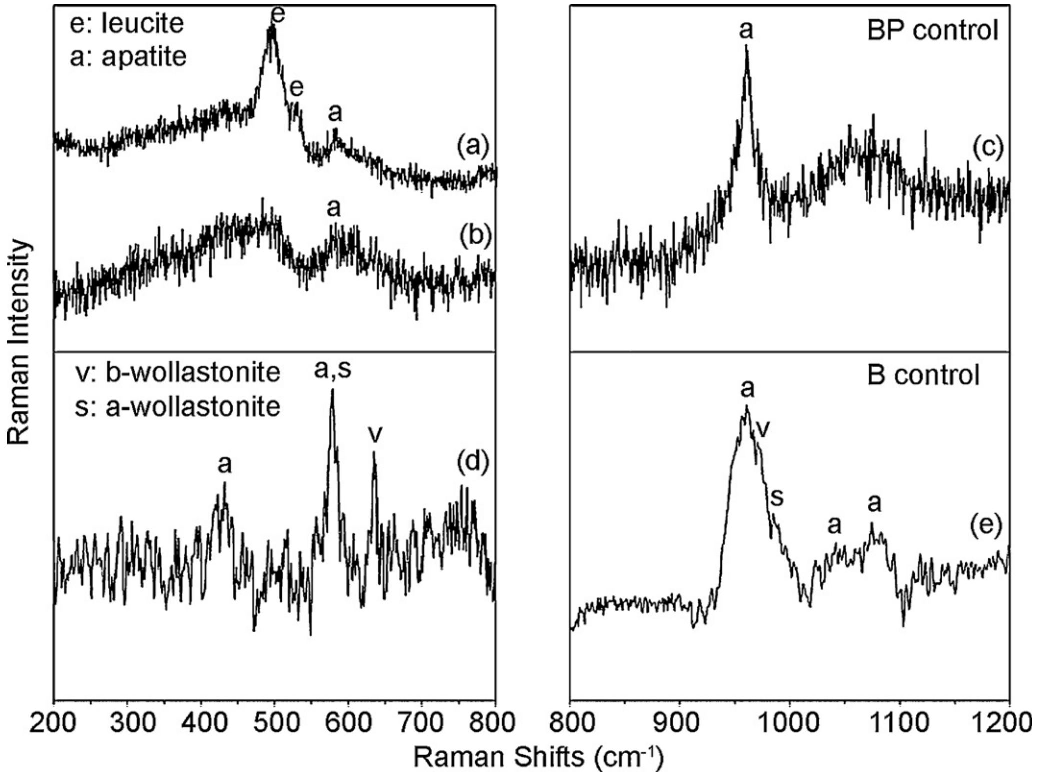

Fig. 4. Raman spectra of BP (a, b, and c) and B (d and e) control specimens.

crystallization of leucite. Despite the fact that the FTIR spectrum of P specimens was dominated by the typical peaks of leucite at 412, 522, 545, 612, 642 and 720 cm^{-1} (Fig. 3c) [18], the contribution of dental porcelain on the FTIR spectrum of the BP specimens was evident by the peak at 642 cm^{-1} (Fig. 3a). Although this peak is shared by both leucite and b-wollastonite, its absence in the FTIR spectrum of the B specimens advocated that it must be attributed to the leucite phase [19]. Raman spectroscopy also supports the aforementioned assignments. As it can be seen, the surface of P specimens exhibits 2 predominant profiles in the Raman spectra, which represented: (a) the amorphous silicate matrix, with two groups of Raman modes at 400–550 and 550–650 cm^{-1}, attributed to the bending vibration of isolated SiO_4 tetrahedra (Fig. 5e) [20], and (b) the leucite phase, distinguished by two peaks positioned at 495 cm^{-1} and 526 cm^{-1} (Fig. 5d), assigned to the T–O–T bending modes (T = Al or Si) [21–23]. Moreover and in accordance with the EDS stoichiometric analysis, typical Raman spectra for the minor crystalline phases of rutile (TiO_2) (Fig. 5a), zinc oxide (ZnO) (Fig. 5a), zirconium oxide (ZrO_2) (Fig. 5b) and casseterite (SnO_2) (Fig. 5a and c) were obtained [24–27]. Beyond leucite, Raman spectroscopy did not identify the minor crystalline phases on the surface of BP specimens, probably due to their low concentration.

3.1.3. XRD analysis

Fig. 6 displays the XR diffractograms of the control specimens. All of them exhibited a broad band located at low diffraction angle (2θ) values, which was indicative of the short range order of the silicate amorphous structure. All the peaks appearing on the XR diffractogram of the P specimens (Fig. 6c), suggested the predominant crystallization of tetragonal (t-) leucite on their surface, while cubic (c-) leucite was represented by the small peak at 26.8° (2θ) [28]. Both types of leucite could also be observed on the XR diffractogram of the BP specimens (Fig. 6a). The predominance of the t- over the c-leucite was due to the reversible temperature dependent leucite phase transformation, which occurs around 620–625 °C [29]. Amount of quartz was also identified by the peak located at 26.3° (2θ) [30]. XRD analysis, also, confirmed the presence of calcium silicate, in terms of a- and b-wollastonite, along with apatite-like phases on both BP and B specimens (Fig. 6a and b). Though, the predominant phase, on the surface of the B specimens, was the a-wollastonite, detected by 3 intense peaks, located at 27.4, 31.7 and 45.7° (2θ). Instead, BP specimens presented an increase of b-wollastonite detected by the relevant peak at 30° (2θ) [31]. A small amount of cristobalite was further identified by the weak peak located at 26.1° (2θ) [32], confirming the indication of FTIR spectrum about SiO_2 crystallization.

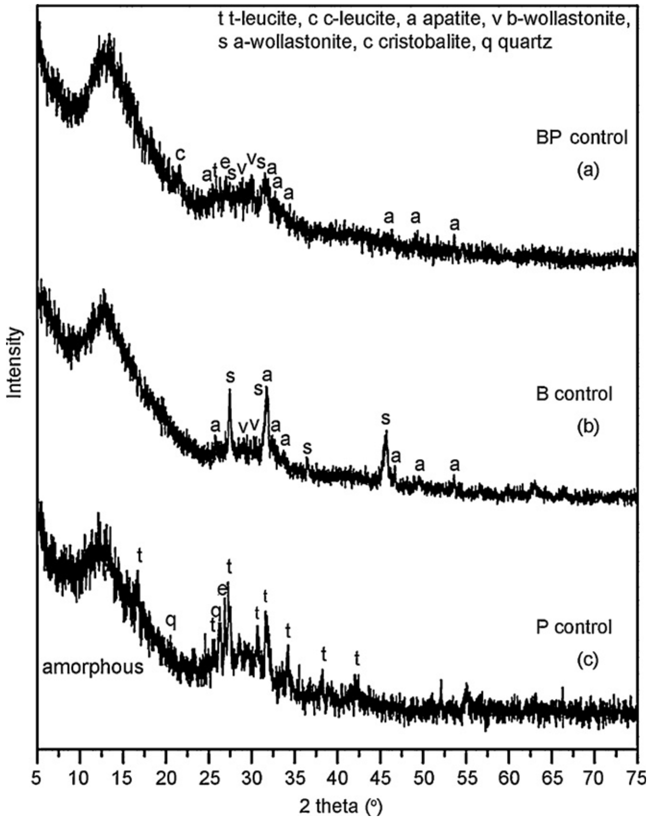

Fig. 6. XRD analysis of BP (a), B (b) and P (c) control specimens.

3.1.4. Porosimetry N_2 analysis

The N_2 adsorption–desorption isotherms of the BP, B and P specimens are presented in Fig. 7. The N_2 adsorption isotherms

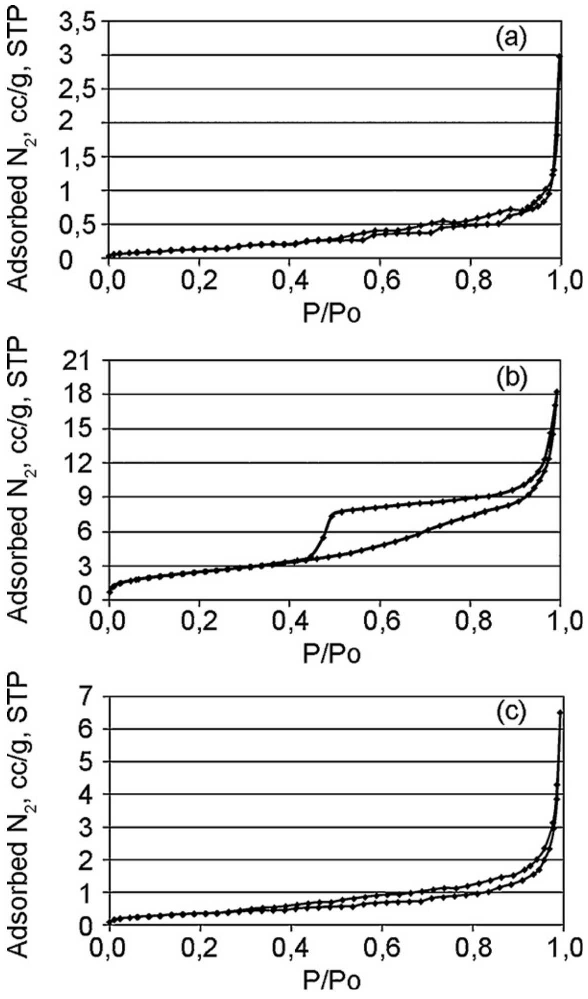

Fig. 7. Adsorption–desorption isotherm plots for BP (a), B (b) and P (c) control specimens.

Table 1
Surface and pore volume of BP, B and P control specimens.

Specimens	Surface area (m^2/g)	Pore volume (cm^3/g)
BP control	1.328	0.010
B control	9.044	0.031
P control	0.545	0.005

of BP (Fig. 7a) and P (Fig. 7c) specimens corresponded to III type, according to IUPAC classification, which is indicative of non-nano- or meso-porous materials. On the contrary, the N_2 adsorption isotherms of B specimens (Fig. 7b) corresponded to the IV or V types, which can be associated with mesoporous materials [33]. Furthermore, the N_2 desorption isotherm for the B specimen exhibited a characteristic hysteresis loop of the H_2 type, which is related to the mechanism of pore filling and emptying. The shape of the loop indicates a ‘‘bottle neck’’ effect during the desorption process. The total pore volume (at $P/P_o = 0.99$; Table 1) is higher for the B specimen (0.031 cc/g), followed by the BP (0.010 cc/g) and the P (0.005 cc/g) specimens. The pore size distribution curve of the B specimen estimated by the BJH method is shown in Fig. 8, since BP and P specimens seemed to be non-porous materials. As it can be seen from the above curve, the majority of the pore diameters is distributed in the range of $2 < D < 50$ nm, thus verifying the mesoporous nature of this sample. Finally, the surface area calculated by the multi-point BET method is higher for the B specimen (20.287 m^2/g), followed by the BP (2.473 m^2/g) and P (1.050 m^2/g) specimens (Table 1).

3.2. Bioactivity analysis

3.2.1. SEM/EDS analysis

Fig. 9 illustrates the surface and cross-section morphologies of the BP specimens, after the immersion in the DMEM solution for 6 days. No evident change was detected at the as-prepared surfaces of the BP specimens until the 3rd day (Fig. 9e), when multiple sites of Ca/P nucleation started to form a thin net-like texture film with spherical particles standing out, which followed the morphology of the substrate's surface. On the 6th day (Fig. 9g), the spherical particles have been agglomerated and the thin film has turned into a dune-like apatite layer with smooth hillocks and deep cracks, which has been reported as the typical image of the apatite layer, without showing any feature of the substrate surface [34]. In the related cross-section images, the apatite layer of the 3rd day was quite thin (4.7–6.7 μm), did not cover the whole surface and did not infiltrate the bulk material (Fig. 9f). Instead, on the 6th day (Fig. 9h), the thickness of apatite layer approached the value of 16.5 μm. The layer was thick enough to be detected and clearly discriminated from the substrate, while it had infiltrated the bulk and covered the external surfaces of the pores. Furthermore, in both the surface and cross-section images, cracks were observed in the apatite layer, which are attributed to the drying of the silica gel, on which the apatite grows. The EDS analysis confirmed, not only the development of apatite layer on the surface, but the infiltration inside the bulk and the pores, by detecting Ca/P ratios of 1.57–2 [35].

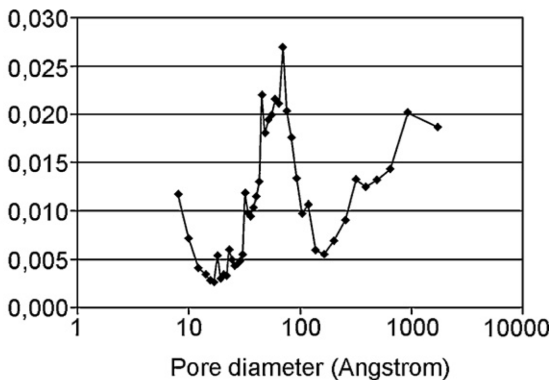

Fig. 8. Diagram of pore size distribution of B control specimen.

3.2.2. FTIR analysis

In Fig. 10, the time-related spectrum changes, detected by the FTIR, with the apatite layer development after the immersion of the BP specimens in DMEM, are presented. Since all the spectra of the BP specimens, before their immersion in DMEM, presented the characteristic phosphate bands of apatite-like phases, located at the 566 and 604 cm^{-1}, the crystallization of biological apatite on specimens surface, after their immersion in DMEM, has been distinguished by the typical peaks of the carbonate groups at: a. 872 cm^{-1} and 1422 cm^{-1}, assigned to the B-type carbonate substitution and b. 1495 cm^{-1}, assigned to the A-type carbonate substitution, all of which were absent at the as-prepared specimen [36]. The carbonate substitution initiated at the 3rd day of incubation for the BP specimens, when the relevant peak intensities were faint. In the course of the 6-day period, the carbonate peaks were progressively becoming more intense, until the 6th day, when they were clearly formed. Furthermore, indicative of the apatite formation at the 3rd and 6th day is the appearance of the 3 peaks at: (a) 1030 cm^{-1}, and 1100 cm^{-1}, which has been assigned to the ν_3PO_4 antisymmetric stretching vibrational mode of the PO_4 groups in the well-crystallized stoichiometric apatite and (b) 960 cm^{-1}, which has been attributed at the ν_1PO_4 [37]. Finally, during the development of apatite layer, on the surface of BP specimens, the peaks, existing at the as-prepared specimens, assigned to the wollastonite and pseudowollastonite, were whittled away toward the 6th day, when they almost disappeared.

3.2.3. XRD analysis

The XRD patterns of the surface of BP specimens after immersion in DMEM, along with the as-prepared specimens are shown in Fig. 11. The XRD spectrum of BP specimens presented 2 weak peaks derived of the broad amorphous band after incubation for 3 days, located at 26.1°, which correspond to the (0 0 2) reflection of apatite phase, and 31.9°, which is the result of the contribution of the (2 1 1), (1 1 2) and (2 0 2) planes of apatite [38]. The amorphous phase has considerably diminished, while the mineral phases existing in the as-prepared BP specimens were almost disappeared until the 6th day of immersion.

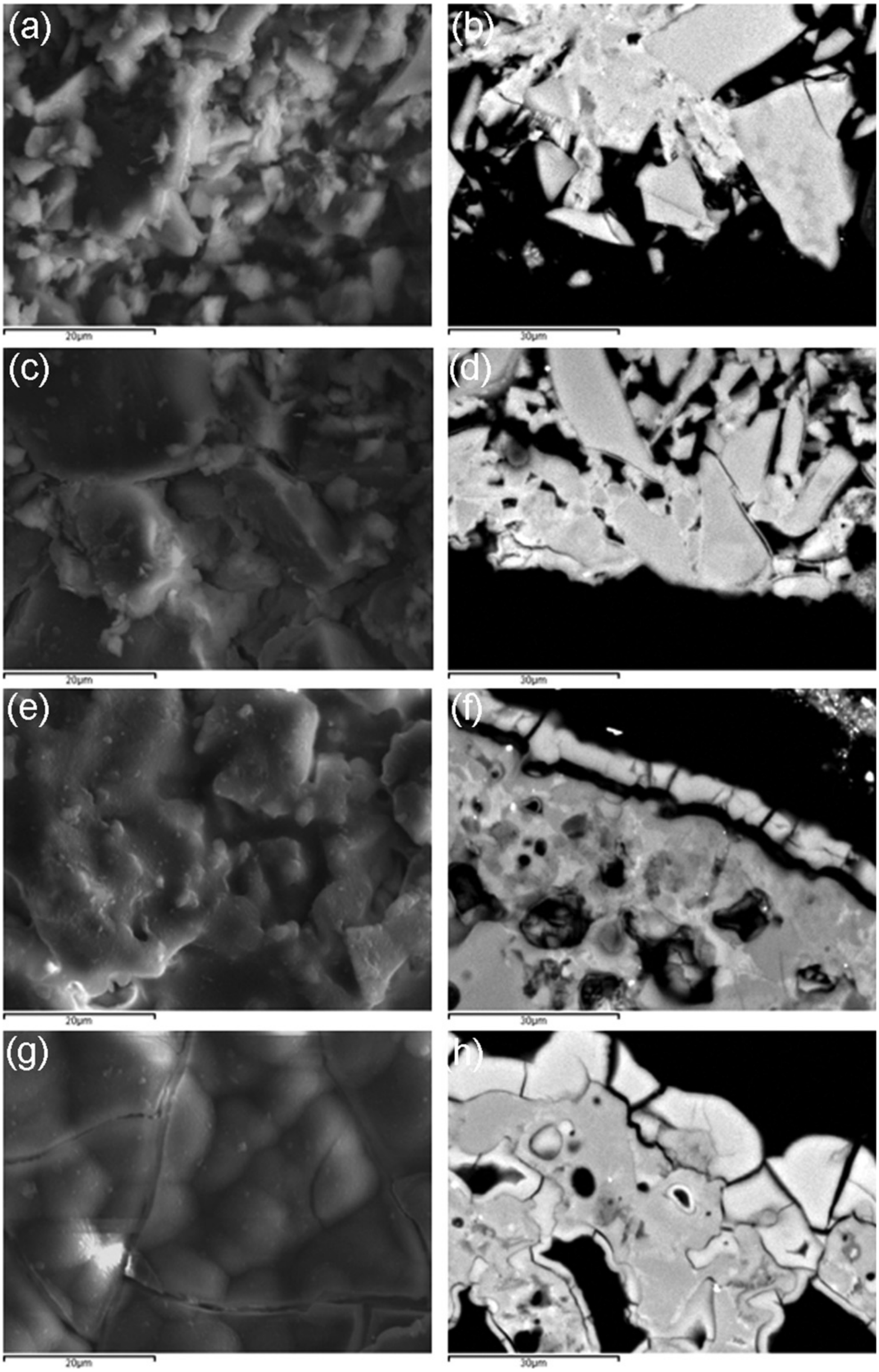

Fig. 9. Secondary surface (a, c, e, and g) and backscatter cross-section (b, d, f, and h) electron analysis 1500× of BP specimens after immersion in DMEM for 6 h (a and b), 1 (c and d), 3 (e and f) and 6 (g and h) days.

4. Discussion

The phase identification of specimens' surface revealed that the 1:1 wt% ratio-contribution of precursors in the initial gel composition of BP composite material along with the sintering temperature of the subsequent firing cycle at 930 °C were effective to favor amorphous glass matrix nucleation yielding mainly Ca–P, Ca–Si and leucite phases, combined with a small

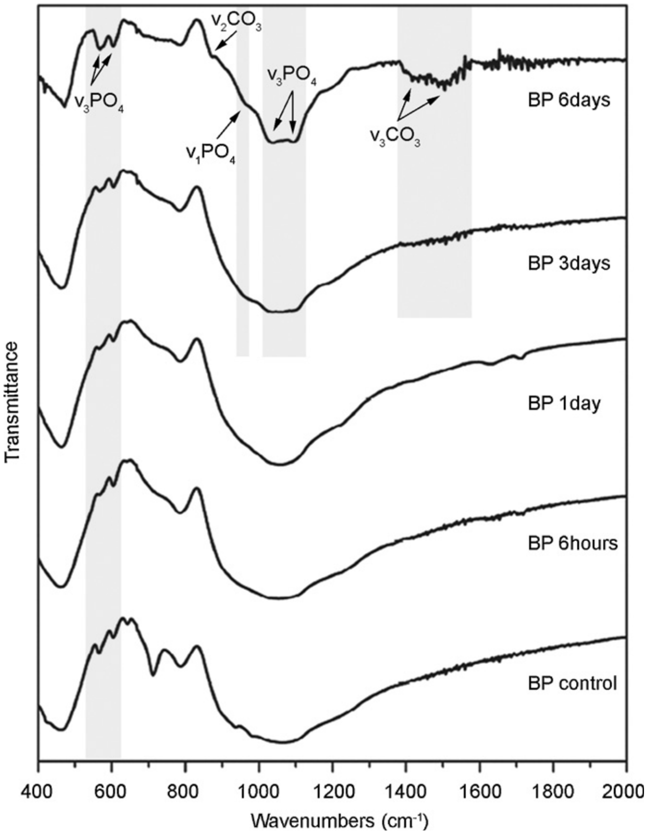

Fig. 10. FTIR analysis of BP specimens after immersion in DMEM for 6 days. Spectrum of as-prepared BP control specimen is included.

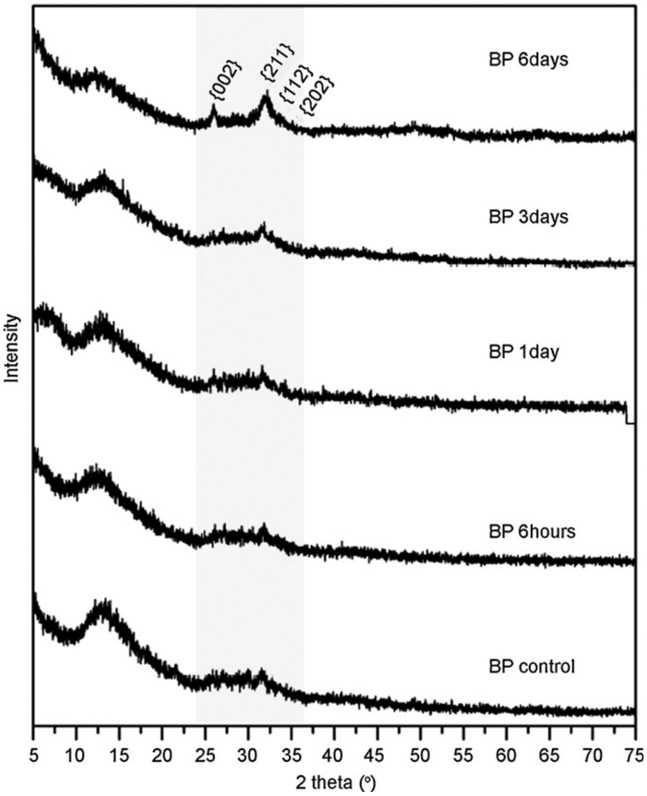

Fig. 11. XRD analysis of BP specimens after immersion in DMEM for 6 days. Spectrum of as-prepared BP control specimen is included.

amount of cristobalite. Beyond the leucite formation, which is the result of dental porcelain in the initial powder material, the formation of these Ca–P phases in the form of apatite-like phases, as it was identified by FTIR, Raman and XRD analysis, seems to be the result of heterogeneous nucleation over dental porcelain grains, acting as foreign initial nuclei, which promote apatite-like crystal nucleation and growth [11]. Additionally, phosphorous ions may substitute for silicon in the tetrahedral coordination in the glasses, while according to Peitl et al., the P=O bond is favorable to phosphate phase formation in a silicate network and thus increases the tendency toward crystallization [39]. The existence Ca–Si phases in the form of a- (pseudo) and b-wollastonite must be attributed to the proximity of the sintering temperature of the firing cycle (930 °C) to the temperature of maximum wollastonite formation (about 950 °C) [40]. At this point, the influence of phosphorous on the crystallization process, which seems to be significant in sol–gel derived glass–ceramics, containing less than 70 mol% of SiO_2 should be highlighted. Specifically, Vallet-Regi et al. reported that phosphorous influenced the phase crystallization on the surface of bioactive ceramics but this effect significantly increased with the SiO_2 content [41]. Furthermore, Padilla et al. concluded that phosphorous induced the crystallization of calcium–phosphate phases, the stabilization of the b-wollastonite phase at high temperature as well as the crystallization of SiO_2 phases at low temperatures, such as cristobalite, which was identified on the surface of the BP specimens in the present study too [42]. As far as the microstructure of the BP specimens is concerned, the adsorption isotherms derived from the N_2 porosimetry along with the cross-section SEM images advocated that the application of the 930 °C sintering temperature during the subsequent firing cycle of the composite specimens resulted in non-nano- or meso-porous material along with low surface energy. Bioactive glass 58S was the only of the investigated specimens, exhibiting mesoporosity, while the ''bottle neck'' effect during the desorption process, as the shape of the loop indicated, should be attributed to the various types of complex pore networks, in which the pore opening is smaller than the pore size. The sharp step on the desorption-isotherm is usually understood as a sign of interconnection of the pores [43,44]. In such systems, the distribution of pore sizes and the pore shape is not well-defined, which is compatible with the SEM observations on B specimens, mentioned above. Furthermore, despite the fact that P specimens presented no nano- or mesoporosity too, the microstructure of the BP specimens was quite different, when compared to the microstructure of the dental porcelain, which presented a homogeneous character with low microporosity. This should be attributed to the surface-driven sintering process of P specimens, during which the particle fusion or the sufficient softening of the glassy material resulted in coherent solids with spherical and small pores [45]. On the contrary, the sinterability of glass–ceramics in the SiO_2–CaO–P_2O_5 system is quite complex [46], since at least 2 crystal phases crystallize on their surface, exhibiting a hindering effect on the sintering kinetics [47,48]. Thus, despite the fact that $T = 930\ ^{\circ}\mathrm{C}$ is recommended as the end-temperature of the firing cycle for the dental porcelain, it is not the appropriate temperature so as for the BP specimens to reach the sintering status, which is desirable for the mechanical strength of the material.

Under the light of the aforementioned analyses of the chemical composition and textural properties, BP composite specimens were evaluated, under dynamic conditions, for their *in vitro* bioactive behavior, since the apatite formation on the material's surface in simulated acellular body fluids is a decisive indicator of their ability to bond to biological tissues [49]. Several authors in the past have reported on the bioactive behavior of dental porcelain modified by 45S bioactive glass, prepared by the high temperature-melting powder preparation technique. The bioactivity of such composite material presented a delayed time of apatite formation, while Kontonasaki et al. declared that the composites with the highest initial amount of bioactive glass precipitated apatite layer on their surface in the immersion time-period of 25–30 days [1]. Instead, the sol–gel preparation technique applied in the present study resulted in a BP composite that in a 3 day-immersion period had already started to precipitate apatite crystals, which, on the 6th day, had turned into a well-defined, thick biological apatite layer not only on the specimens' surface but inside the pores, too. The rationale beyond the faster surface reactivity of the sol–gel derived BP specimens lies on the bioactivity index of the crystal phases developed during the preparation process and the firing cycle. More specifically, both wollastonite and pseudowollastonite have similar composition to that of $CaO–SiO_2$-based bioactive glasses and glass–ceramics, thus, the apatite formation may in principle be explained by the same reaction mechanism [50–52]. When the BP specimens are immersed in the solution, dissolved calcium ions (Ca^{++}) from the wollastonite crystal structure are exchanged with hydrogen ions (H^{-}), leading to the production of a negatively charged layer, which may attract Ca^{++} from the solution and promote apatite precipitation. Furthermore, this initial $Ca^{++}–H^{-}$ exchange transforms wollastonite into an amorphous silicate matrix with higher bioactivity index [53]. In the literature, there are studies, investigating the bioactivity of glass–ceramics, which crystallize wollastonite on the surface of specimens, suggesting that the presence of wollastonite favors the faster precipitation of apatite crystals, when compared to other glass or glass–ceramics with different composition [54]. Furthermore, pseudowollastonite, which is a crystal polymorph of wollastonite [55], is considered the dissolved crystal phase with the higher rate of apatite formation. Despite the fact that pseudowollastonite presents the same reaction mechanism to wollastonite, its surface dissolution rate is much higher [42,56]. A comparative study, investigating the bioactive behavior of diopside ceramics, inferred that those that contained pseudowollastonite induced bioactivity quite faster that those that contained wollastonite [57]. The results of the present study confirmed the aforementioned data, since the FTIR peaks assigned to wollastonite and pseudowollastonite tend to whittle away toward the 6th day of immersion, when apatite has already been formed. However, despite the fact that the sol–gel derived BP specimens exhibited much faster surface reactivity compared to the melt-derived ones, the reaction mechanism rather delayed (days) compared to the time required for the *in vivo* healing process to initiate (hours). The former may be attributed to the presence of cristobalite, leucite and apatite phases on the BP specimens' surface, which are considered to retard the apatite formation compared to the Ca–Si phases. In particular, the leucite crystals present low index of bioactivity, since it has been reported that no apatite layer has been detected on the melt-derived composites with the highest proportion of dental ceramic for the immersion time of 45 days [1], while recent research, studying the bioactivity of sol–gel derived powder composite material, demonstrated that the time of apatite development increased as a function of the leucite content [58]. The presence of cristobalite has been previously detected as a resultant phase of the glass or glass–ceramics based on the $CaO–SiO_2–P_2O_5$ oxide system, while its ability to induce bioactivity has not been investigated. However, a study investigating the *in vitro* protein absorption on a $CaO–SiO_2–P_2O_5$-based glass–ceramic resulted in the enhancement of bioactivity as the temperature increased and the crystals of quartz were transformed into cristobalite [59]. This could be assigned to the comparatively open atomic tetragonal structure with less degree of symmetry along with the increased crystal defect, when treated at higher temperature (above 800 °C) [60,61]. Additionally, stoichiometric apatite crystals present lower bioactivity index compared to wollastonite [54], while others argue that apatite does not accelerate the precipitation of biological apatite after immersion [62]. Finally, beyond chemical composition, microstructure in terms of porosity and surface area is likely to affect dissolution properties of the material and biological activity. It has been declared that bioactive behavior may be exhibited by nano- or meso-porous materials with surface area larger than $40–80\ m^2/g$ [63]. In the present study, the BP composite material presented by far lower surface area compared to the indicated, while, as it was mentioned above, it did not present any nano- or micro-porosity. This may justify the delayed time of apatite formation. Nevertheless, it should be mentioned, in the literature, there are studies indicating that materials with surface area even less than $1\ m^2/g$ may exhibit sufficient bioactivity, due to the textural properties that they develop after their immersion in the solution. More specific, surfaces of high dissolution rate develop faster release of Ca^{++} after their immersion, which may alter the textural properties of the material, by increasing both porosity and surface area [64–66].

5. Conclusions

Under the limitations of the present study, the modification of the sol–gel derived dental porcelain by bioactive glass seems to be a significantly improved composite as far as the bioactive behavior is concerned, compared to other materials of the same oxide system. However, the time of the *in vitro* bioactivity induction, which is related to the time of *in vivo* tissue response, should be further reduced, indicating that further modifications need to be considered in order to fulfill the requirements of application in the clinical reality.

References

[1] E. Kontonasaki, N. Kantiranis, X. Chatzistavrou, L. Papadopoulou, K.M. Paraskevopoulos, P. Koidis, Studying dental ceramic-bioactive glass composites, Key Engineering Materials 361–363 (2008) 881–884.

[2] E. Kontonasaki, A. Sivropoulou, L. Papadopoulou, P. Garefis, K.M. Paraskevopoulos, P. Koidis, Attachment and proliferation of human periodontal ligament fibroblasts on bioactive glass modified ceramics, Journal of Oral Rehabilitation 34 (2007) 57–67.

[3] P. Sepulveda, J.R. Jones, L.L. Hench, Characterization of melt-derived 45S5 and sol–gel-derived 58S bioactive glasses, Journal of Biomedical Materials Research 58 (2001) 734–740.

[4] P. Sapuvelda, J.R. Jones, L.L. Hench, In vitro dissolution of melt-derived 45S5 and sol–gel derived 58S bioactive glasses, Journal of Biomedical Materials Research 61 (2002) 301–311.

[5] D. Acros, D.C. Greenspan, M. Vallet-Regi, Influence of the stabilization temperature on textural and structural features and ion release SiO_2–CaO–P_2O_5 sol–gel glasses, Chemistry of Materials 14 (2002) 1515–1522.

[6] R. Li, A.E. Clark, L.L. Hench, An investigation of bioactive glass powders by sol–gel processing, Journal of Applied Biomaterials 2 (1991) 231–239.

[7] J. Zhong, D.C. Greenspan, Processing and properties of sol–gel bioactive glasses, Journal of Biomedical Materials Research 63 (2001) 694–701.

[8] A.J. Salinas, A.I. Martin, M. Vallet-Regi, Bioactivity of three CaO–P_2O_5–SiO_2 sol–gel glasses, Journal of Biomedical Materials Research 61 (2002) 524–532.

[9] A.J. Salinas, M. Vallet-Regi, The sol–gel production of bioceramics, Key Engineering Materials 391 (2008) 141–158.

[10] X. Chatzistavrou, D. Esteve, E. Hatzistavrou, E. Kontonasaki, K.M. Paraskevopoulos, A.R. Boccaccini, Sol–gel based fabrication of novel glass–ceramics and composites for dental applications, Materials Science and Engineering 30 (2010) 730–739.

[11] O.M. Goudouri, E. Kontonasaki, A. Theoharidou, L. Papadopoulou, N. Kantiranis, X. Chatzistavrou, P. Koidis, K.M. Paraskevopoulos, Modifying a dental ceramic by bioactive glass via the sol–gel route: characterization and bioactivity investigation, Materials Chemistry and Physics 125 (2011) 309–313.

[12] X. Chatzistavrou, T. Zorba, E. Kontonasaki, K. Chrissafis, P. Koidis, K.M. Paraskevopoulos, Following bioactive glass behavior beyond melting temperature by thermal and optical methods, Physical Status Solidi A 201 (2004) 944–951.

[13] A. Balamurugan, J. Michel, J. Faure, H. Benhayoune, L. Wortham, G. Sockalingum, V. Banchet, S. Bouthors, D. Laurent-Maquin, G. Balossier, Synthesis and structural analysis of sol gel derived stoichiometric monophasic hydroxyapatite, Ceramics-Silikaty 50 (2006) 27–31.

[14] V.A. Sinyayev, E.S. Shustikova, D. Griggs, D.V. Dorofeev, The nature of P–O bonds in the precipitated amorphous calcium phosphates and calcium magnesium phosphates, Glass Physics and Chemistry 31 (2005) 671–675.

[15] J. Ma, C.Z. Chen, D.G. Wang, X.G. Meng, J.Z. Shi, Influence of the sintering temperature on the structural feature and bioactivity of sol–gel derived SiO_2–CaO–P_2O_5 bioglass, Ceramics International 36 (2010) 1911–1916.

[16] E. Huang, C.H. Chen, T. Huang, E.H. Lin, Xu F J., Raman spectroscopic characteristics of Mg–Fe–Ca pyroxenes, American Mineralogist 85 (2000) 473–479.

[17] J.M. Fernandez-Prada, P. Serra, J.L. Morenza, P.N. De Aza, Pulsed laser deposition of pseudowollastonite coatings, Biomaterials 23 (2002) 2057–2061.

[18] S. Music, J. Zivko-Babic, K. Mehulic, M. Ristic, S. Popovic, K. Furic, Microstructure of lucite glass–ceramics for dental use, Materials Letters 27 (1996) 195–199.

[19] O.M. Goudouri, E. Kontonasaki, N. Kantiranis, X. Chatzistavrou, L. Papadopoulou, P. Koidis, K.M. Paraskevopoulos, A bioactive glass/dental porcelain system by the sol gel route: fabrication and characterization, Key Engineering Materials 396–398 (2009) 95–98.

[20] L. Marsich, L. Moimas, V. Sergo, C. Schmid, Raman spectroscopic study of bioactive silica-based glasses: the role of the alkali/alkali earth ratio on the non-bridging oxygen/bridging oxygen (NBO/BO) ratio, Spectroscopy 23 (2009) 227–232.

[21] N. Ovsyuka, S. Goryainov, Amorphous-to-amorphous phase transition in zeolites, JETP Letters 83 (2006) 138–142.

[22] M. Castriota, V. Cosco, T. Barone, G. De Santo, P. Carafa, E. Cazzanelli, Micro-Raman characterizations of Pompei's mortars, Journal of Raman Spectroscopy 39 (2008) 295–301.

[23] D.A. McKeown, A.C. Buechele, C. Viragh, I.L. Pegg, Raman and X-ray absorption spectroscopic studies of hydrothermally altered alkali-borosilicate nuclear waste glass, Journal of Nuclear Materials 399 (2010) 13–25.

[24] A.D. Barros, K.F. Albertin, J. Miyoshi, I. Doi, J.A. Diniz, Thin titanium oxide films deposited by e-beam evaporation with additional rapid thermal oxidation and annealing for ISFET applications, Microelectronic Engineering 87 (2010) 443–446.

[25] G.G. Siu, M.J. Stokes, Y. Liu Y, Variation of fundamental and higher-order Raman spectra of ZrO_2 nanograins with annealing temperature, Physical Review B 59 (1999) 3173–3179.

[26] K.E. Rammutla, A.V. Chadwick, J. Harding, D.C. Sayle, R.M. Erasmus, EXAFS and Raman scattering studies of Y and Zr doped nano-crystalline tin oxide, Journal of Physics: Conference Series 249 (2010) 1–5.

[27] K. McGuire, Z.W. Pan, Z.L. Wang, D. Milkie, I. Menéndez, A.M. Rao, Raman studies of semiconducting oxide nanobelts, Journal of Nanoscience and Nanotechnology 5 (2002) 499–502.

[28] I.L. Denry, J.A. Holloway, H.O. Colijn, Phase transformations in a leucite-reinforced pressable dental ceramic, Journal of Biomedical Materials Research 54 (2001) 351–359.

[29] M. Novotna, J. Maixner, X-ray diffraction study of leucite crystallization, Zeitschrift für Kristallographie Supplement 23 (2006) 455–459.

[30] R.T. Downs, K.L. Bartelmehs, G.V. Gibbs, M.B. Boysen Jr., Interactive software for calculating and displaying X-ray or neutron powder diffractometer patterns of crystalline materials, American Mineralogist 78 (1993) 1104–1107.

[31] M.S. Hernández-Crespo, M. Romero, J.M. Rincón, Nucleation and crystal growth of glasses produced by a generic plasma arc-process, Journal of the European Ceramic Society 26 (2006) 1679–1685.

[32] Y. Shinohara, N. Kohyama, Quantitative analysis of tridymite and cristobalite crystallized in rice husk ash by heating, Industrial Health 42 (2004) 277–285.

[33] J. Rouquerol, D. Avnir, C.W. Fairbridge, D.H. Everett, J.M. Haynes, N. Pernicone, J.D.F. Ramsay, K.S.W. Sing, K.K. Unger, Recommendations for the characterization of porous solids (technical report), Pure and Applied Chemistry 66 (1994) 1739–1758.

[34] J. Weng, Q. Liu, J.G.C. Wolke, X. Zhang, K. de Groot, Formation and characteristics of the apatite layer on plasma-sprayed hydroxyapatite coatings in simulated body fluid, Biomaterials 18 (1997) 1027–1035.

[35] A. Ito, K. Onuma, Growth of hydroxyapatite crystals, in: B. Byreppa (Ed.), Crystal Growth Technology, William Andrew Publishing/Noyes, Norwich, NY, 2003, pp. 525–559.

[36] T. Leventouri, A. Antonakos, A. Kyriacou, R. Venturelli, E. Liarokapis, V. Perdikatsis, Crystal structure studies of human dental apatite as a function of age, International Journal of Biomaterials (2009) 1–6. , http://dx.doi.org/10.1155/2009/698547.

[37] D. Farlay, G. Panczer, C. Rey, P. Delmas, G. Boivin, Mineral maturity and crystallinity index are distinct characteristics of bone, Journal of Bone and Mineral Metabolism 28 (2010) 433–445.

[38] Y.F. Chou, W.A. Chiou, Y. Xu, J.C. Dunn, B.M. Wu, The effect of pH on the structural evolution of accelerated biomimetic apatite, Biomaterials 25 (2004) 5323–5331.

[39] O. Peitl Filho, G.P. LaTorre, L.L. Hench, Effect of crystallization on apatite-layer formation of bioactive glass 45S5, Journal of Biomedical Materials Research 30 (1996) 509–514.

[40] R.P. Chakradhar Sreekanth, B.M. Nagabhushana, G.T. Chandrappa, K.P. Ramesh, J.L. Rao, Solution combustion derived nanocrystalline macroporous wollastonite ceramics, Materials Chemistry and Physics 95 (2006) 169–175.

[41] M. Vallet-Regi, J. Roman, S. Padilla, J.C. Doadrio, F.J. Gil, Bioactivity and mechanical properties of SiO_2–CaO–P_2O_5 glass–ceramics, Journal of Materials Chemistry 15 (2005) 1353–1359.

[42] S. Padilla, J. Román, A. Carenas, M. Vallet-Regí, The influence of the phosphorus content on the bioactivity of sol–gel glass ceramics, Biomaterials 26 (2005) 475–483.

[43] G. Masin, G.D. Yadav, Capillary hysteresis in the pore space of a packing of spheres measured by the movement of blobs, Journal of Colloid and Interface Science 95 (1983) 120–130.

[44] P.I. Ravikovitch, A.V. Neimark, Experimental confirmation of different mechanisms of evaporation from ink-bottle type pores: equilibrium, pore blocking, and cavitation, Langmuir 18 (2002) 9830–9837.

[45] K.C. Cheung, B.W. Darvell, Sintering of dental porcelain: effect of time and temperature on appearance and porosity, Dental Materials 18 (2002) 163–173.

[46] M.O. Prado, M.L.F. Nascimento, E.D. Zanotto, On the sinterability of crystallizing glass powders, Journal of Non-Crystalline Solids 354 (2008) 4589–4597.

[47] M.O. Prado, C. Fredericci, E.D. Zanotto, Non-isothermal sintering with concurrent crystallization of polydispersed soda–lime–silica glass beads, Journal of Non-Crystalline Solids 331 (2003) 157–167.

[48] Q. Fu, M.N. Rahaman, B.S. Bal, W. Huang, D.E. Day, Preparation and bioactive characteristics of a porous 13–93 glass, and fabrication into the articulating surface of a proximal tibia, Journal of Biomedical Materials Research Part A 82 (2007) 222–229.

[49] M.P. Ferraz, F.J. Monteiro, J.D. Santos, Cao–P_20_5 glass hydroxyapatite double-layer plasma sprayed coating: in vitro bioactivity evaluation, Journal of Biomedical Materials Research 45 (1999) 376–383.

[50] X. Liu, C. Ding, Apatite formed on the surface of plasma sprayed wollastonite coatings immersed in simulated body fluids, Biomaterials 22 (2001) 2007–2012.

[51] X. Liu, C. Ding, P.K. Chu, Mechanism of apatite formation on wollastonite coatings in simulated body fluids, Biomaterials 25 (2004) 1755–1761.

[52] X. Liu, C. Ding, Reactivity of plasma sprayed wollastonite in simulated body fluid, Journal of Biomedical Materials Research 59 (2002) 259–264.

[53] P.N. De Aza, Z. Luklinska, M.R. Anseau, F. Guitian, S. De Aza, Reactivity of wollastonite–tricalcium phosphate bioeutectic ceramic in human parotid saliva, Biomaterials 21 (2000) 1735–1741.

[54] K. Lin, M. Zhang, W. Zhai, H. Qu, J. Chang, Fabrication and characterization of hydroxyapatite/wollastonite composite bioceramics with controllable properties for hard tissue repair, Journal of the American Ceramic Society 94 (2011) 99–105.

[55] L.M. Rodriguez-Lorenzo, R. GarcIa-Carrodeguas, M.A. RodrIguez, S. De Aza, J. Jimenez, A. Lopez-Bravo, M. Fernandez, J.S. Roman, Synthesis characterization, bioactivity and biocompatibility of nanostructured materials based on the wollastonite–poly(ethylmethacrylate-covinylpyrrolidone) system, Journal of Biomedical Materials Research Part A 88 (2009) 53–64.

[56] J. Roman, S. Padilla, M. Vallet-Regi, Sol–gel glasses as precursors of bioactive glass–ceramics, Chemistry of Materials 15 (2003) 798–806.

[57] M.A. Sainz, P. Pena, S. Serena, A. Caballero, Influence of design on bioactivity of novel $CaSiO_3$–$CaMg(SiO_3)_2$ bioceramics: in vitro simulated body fluid test and thermodynamic simulation, Acta Biomaterials 6 (2010) 2797–2807.

[58] O.M. Goudouri, E. Kontonasaki, A. Theocharidou, L. Papadopoulou, X. Chatzistavrou, P. Koidis, K.M. Paraskevopoulos, In vitro bioactivity studies of sol–gel derived dental ceramics/bioactiveglass composites in periodically renewed biomimetic solution, Bioceramics Development and Applications 1 (2011) 1–4.

[59] C.Q. Ning, J. Mehta, A. El-Ghannam, Effects of silica on bioactivity of calcium phosphates composites immersed in vitro, Journal of Materials Science: Materials in Medicine 16 (2005) 355–360.

[60] G.D. Guthrie, P.J. Heaney, Mineralogical characteristics of silica polymorphs in relation to their biological activities, Scandinavian Journal of Work, Environment & Health 2 (2005) 5–8.

[61] A.R. El-Ghannam, Advanced bioceramic composite for bone tissue engineering: design principles and structure–bioactivity relationship, Journal of Biomedical Materials Research Part A 69 (2004) 490–501.

[62] O. Peitl, E. Dutra Zannotto, L.L. Hench, Highly bioactive P_2O_5–Na_2O–CaO–SiO_2 glass–ceramics, Journal of Non-Crystalline Solids 292 (2001) 115–126.

[63] J.P. Zhong, D.C. Greenspan, J.W. Feng, A microstructural examination of apatite induced by Bioglass$^{®}$ in vitro, Journal of Materials Science: Materials in Medicine 13 (2002) 321–326.

[64] A. Oliveira Paiva, M.G. Duarte, M.H.V. Fernandes, M.H. Gil, N.G. Costa, In vitro studies of bioactive glass/polyhydroxybutyrate composites, Materials Research 9 (2006) 417–423.

[65] M. Vallet-Regi, D. Arcos, J. Perez-Pariente, Evolution of porosity during in vitro hydroxycarbonate apatite growth in sol–gel glasses, Journal of Biomedical Materials Research 51 (2000) 23–28.

[66] M. Vallet-Regi, Ceramics for medical applications, Journal of the Chemical Society, Dalton Transactions 2 (2001) 97–108.